MDPI

Article

Assessing the Effect of Real Spatial Resolution of In Situ UAV Multispectral Images on Seedling Rapeseed Growth Monitoring

Jian Zhang [1,2,†] , **Chufeng Wang** [1,2,†], **Chenghai Yang** [3] , **Tianjin Xie** [1,2], **Zhao Jiang** [1,2], **Tao Hu** [1,2], **Zhibang Luo** [1,2], **Guangsheng Zhou** [4] and **Jing Xie** [5,*]

[1] Macro Agriculture Research Institute, College of Resource and Environment, Huazhong Agricultural University, 1 Shizishan Street, Wuhan 430070, China; Jz@mail.hzau.edu.cn (J.Z.); cfwang@webmail.hzau.edu.cn (C.W.); purple@webmail.hzau.edu.cn (T.X.); jzh@webmail.hzau.edu.cn (Z.J.); Hutao@webmail.hzau.edu.cn (T.H.); luozb@webmail.hzau.edu.cn (Z.L.)
[2] Key Laboratory of Farmland Conservation in the Middle and Lower Reaches of the Ministry of Agriculture, Wuhan 430070, China
[3] Aerial Application Technology Research Unit, USDA-Agricultural Research Service, College Station, TX 77845, USA; chenghai.yang@ars.usda.gov
[4] College of Plant Science and Technology, Huazhong Agricultural University, Wuhan 430070, China; zhougs@mail.hzau.edu.cn
[5] College of Science, Huazhong Agricultural University, Wuhan 430070, China
[*] Correspondence: xiejing625@mail.hzau.edu.cn
[†] These authors contributed equally to this work.

check for updates

Abstract: The spatial resolution of in situ unmanned aerial vehicle (UAV) multispectral images has a crucial effect on crop growth monitoring and image acquisition efficiency. However, existing studies about optimal spatial resolution for crop monitoring are mainly based on resampled images. Therefore, the resampled spatial resolution in these studies might not be applicable to in situ UAV images. In order to obtain optimal spatial resolution of in situ UAV multispectral images for crop growth monitoring, a RedEdge Micasense 3 camera was installed onto a DJI M600 UAV flying at different heights of 22, 29, 44, 88, and 176m to capture images of seedling rapeseed with ground sampling distances (GSD) of 1.35, 1.69, 2.61, 5.73, and 11.61 cm, respectively. Meanwhile, the normalized difference vegetation index (NDVI) measured by a GreenSeeker (GS-NDVI) and leaf area index (LAI) were collected to evaluate the performance of nine vegetation indices (VIs) and VI*plant height (PH) at different GSDs for rapeseed growth monitoring. The results showed that the normalized difference red edge index (NDRE) had a better performance for estimating GS-NDVI ($R^2 = 0.812$) and LAI ($R^2 = 0.717$), compared with other VIs. Moreover, when GSD was less than 2.61 cm, the NDRE*PH derived from in situ UAV images outperformed the NDRE for LAI estimation ($R^2 = 0.757$). At oversized GSD (≥ 5.73 cm), imprecise PH information and a large heterogeneity within the pixel (revealed by semi-variogram analysis) resulted in a large random error for LAI estimation by NDRE*PH. Furthermore, the image collection and processing time at 1.35 cm GSD was about three times as long as that at 2.61 cm. The result of this study suggested that NDRE*PH from UAV multispectral images with a spatial resolution around 2.61 cm could be a preferential selection for seedling rapeseed growth monitoring, while NDRE alone might have a better performance for low spatial resolution images.

1. Introduction

Nowadays, the food security challenge has become a major concern for many countries and regions in the light of changing climatic conditions, political instabilities, and increasing consumption of resources [1]. In order to ensure the stability of food production, it is important for farmers to quickly and accurately obtain crop growth information in the field and take effective measures accordingly [2]. Traditionally, crop growth information such as leaf area index (LAI) [3] and biomass [4] is mainly obtained by manual destructive sampling methods, which are time-consuming. Nowadays, many studies have reported that GreenSeeker (GS), ASD handheld spectrometers, plant canopy analyzer and other field-based remote sensing sensors can accurately acquire the normalized difference vegetation index (NDVI), LAI and other biophysical parameters related to crop growth [5–8]. However, these methods still require manual operation and are labor-intensive for extensive sampling processes. Airborne and spaceborne remote-sensing technologies have been applied to a wide range of crop growth monitoring for decades [9], but the image resolution from this technology is too low to measure crop growth on fine scales [10].

In recent years, the rapid development of unmanned aerial vehicle (UAV) remote sensing technology has provided an effective way of accurately obtaining crop growth information on a plot level. The imaging sensors mounted on the UAV mainly include hyperspectral, RGB, and multispectral sensors. They were reported to have a great performance for monitoring crop growth [11–16]. Compared with the former two, UAV-based multispectral sensors can acquire images with a spatial resolution from centimeter to decimeter level near the ground, achieving a better balance between cost and availability [17]. In previous studies, red edge (RE) and near infrared (NIR) vegetation indices (VIs) extracted from UAV multispectral images have been confirmed to be capable of precisely estimating crop-growth-related parameters such as the leaf area index (LAI) of wheat [18] and nitrogen status of rapeseed [19].

Ground sampling distance (GSD) was used to measure the spatial resolution of images. In previous studies, the impact of GSD on the estimation of plant biophysical parameters has rarely been discussed. However, GSD is crucial for the spectroscopic estimation of plant biochemical variables and affects the efficiency in UAV image acquisition [20]. Some studies have assessed the performance of VIs from images with different GSDs for estimating the leaf nitrogen concentration of rice [20] and the leaf chlorophyll content of sugar beet [21]. However, the images with different GSDs in these studies were obtained by resampling high-resolution images, so the conclusion based on resampled images might not be suitable for assessing the performance of VIs from in situ UAV images. In addition, VIs, combined with plant height (PH) from digital surface models (PH_{DSM}), have also been utilized to estimate crop biomass to achieve higher accuracy [22–24]. The GSD of the UAV images is closely related to the accuracy of the PH_{DSM} acquisition, thus affecting the crop growth estimation by $VI*PH_{DSM}$ (product of VI and PH_{DSM}). The GSD of the image depended mainly on the sensor's field of view (FOV) and the height of the observation platform. Images with larger GSDs were collected at higher flight altitudes, which could improve the efficiency of in situ UAV image acquisition and processing. However, oversized GSDs might result in instability for the spectroscopic estimation of biochemical variables [25] and PH estimation [26]. Therefore, it is of great importance to determine an optimal spatial resolution by sensitivity analyses and to achieve a balance between the measurement accuracy and measurement efficiency of in situ UAV images [27].

It is necessary to use field-based data as a reference, in order to evaluate the performance of in situ UAV images for estimating crop-growth-related parameters [28]. Ground-based sensors such as GreenSeeker and leaf area canopy analyzers are often used to obtain the NDVI (GS-NDVI) and LAI of crop canopy. GS-NDVI is measured by active remote sensing, and not affected by shadows and changes in lighting environments [29]. Therefore, the GS-NDVI is reliable in the inversion of crop growth parameters such as the yield of corn [30] and nitrogen content of rice [31]. LAI is an important indicator for describing vegetation biophysical processes such as photosynthesis [32].

Based on the above knowledge, the individual VIs and VIs*PH$_{DSM}$ derived from in situ UAV images with different GSDs were utilized to estimate the GS-NDVI and LAI of seedling rapeseed in our study. On this basis, the difference between VIs from the in situ UAV images and those from resampled images was discussed and the impact of spatial resolution on PH extraction accuracy and VI generation was analyzed according to the semivariogram. Finally, an optimal spatial resolution was determined to achieve a balance between the measurement accuracy and measurement efficiency of in situ UAV images.

2. Materials and Methods

2.1. Study Area

The study area (Figure 1) is located on the experiment station of Huazhong Agricultural University, Wuhan City, Hubei Province (30°28′8″ N, 114°21′18″ E). Three experiments were performed in 180 plots over the study area with each plot covering an area of 10 m^2 (5.0 × 2.0 m). Each treatment of the three experiments was performed in triplicates.
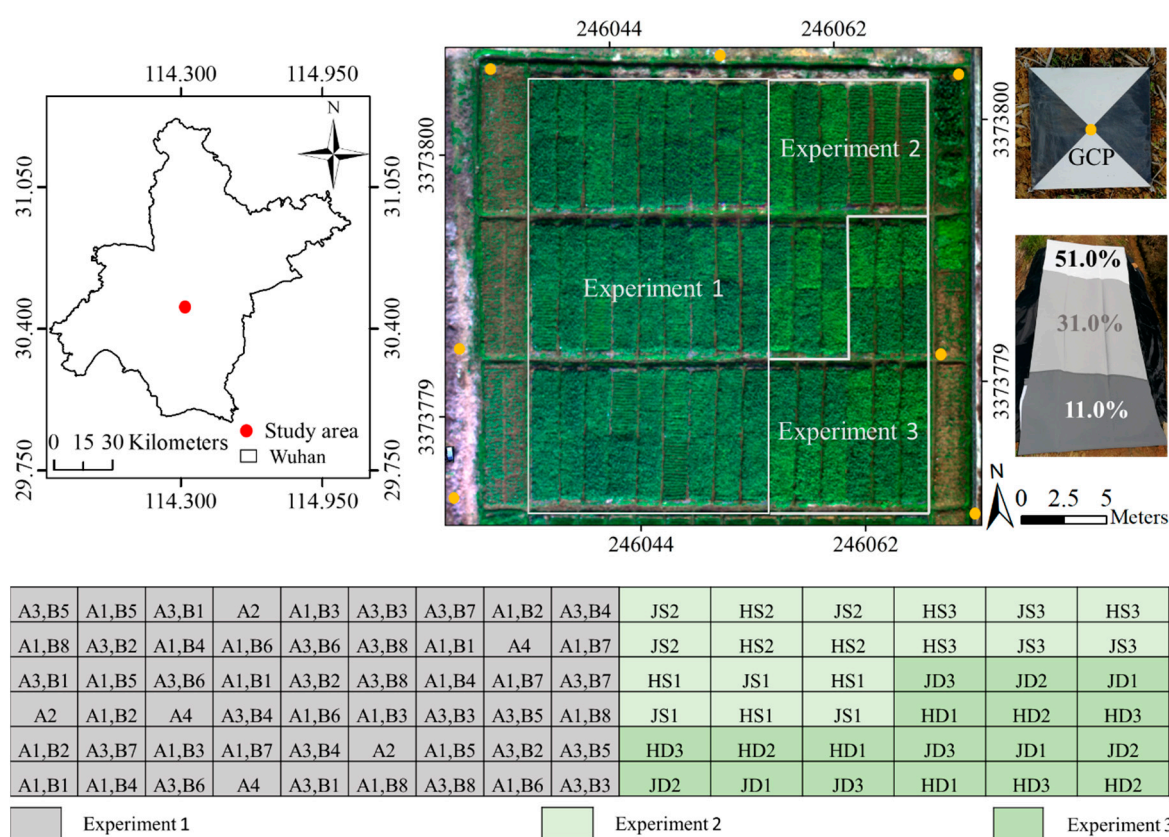

Figure 1. Layout of study area. The white lines were the boundary of study areas of Experiments 1, 2 and 3. The orange dots indicated the locations of ground control points (GCPs). The 11.0%, 31.0% and 51.0% were the reflectance of calibration targets.

The first was a straw incorporation experiment on the rapeseed cultivar of "Huayouza No. 62". Four treatments were set in this experiment: incorporating straw and fertilizing (A1), incorporating straw and not fertilizing (A2), not incorporating straw and fertilizing (A3), and not incorporating straw and not fertilizing (A4). The planting density was 50,000 plants/ha and the amount of straw was 800 kg/ha. Eight N fertilization treatments were set for the full growth stage. The rates of basal fertilizer:tiller fertilizer:overwinter fertilizer:flower fertilizer were 100%:0:0:0 (B1), 60%:40%:0:0 (B2), 60%:0:40%:0 (B3), 60%:0:0:40% (B4), 60%:20%:20%:0 (B5), 60%:20%:0:20% (B6), 60%:0:20%:20% (B7),

60%:40%:0:0 (B8). In the first seven treatments, the amount of N fertilization (urea) was 16 kg/ha. In the eighth treatment, the amount of N fertilization application was 20 kg/ha. However, only the basal fertilizer and tiller fertilizer were applied before the UAV data collection.

In the second experiment, the rapeseed cultivars of "Huayouza No. 62 (H)" and "Juayouza No. 158 (J)" were sown on three different dates (20 September (S1), 1 October (S2), 10 October 2018 (S3)) with a planting density of 30,000 plants/ha. In the third experiment, the same two rapeseed cultivars were sown on 28 September 2018 with three different densities (30,000 plants/ha (D1), 40,000 plants/ha (D2), and 50,000 plants/ha (D3)). Only the basal fertilizer and tiller fertilizer were applied in the second and third experiment. The basal fertilizer was the compound fertilizer with an amount of 50 kg/ha. The till fertilizer was the N fertilization (urea) with amount of 10 kg/ha.

For image mosaicking and rectification, seven ground control points (GCPs) were distributed evenly in the study area (Figure 1). The position information of GCPs was collected with a global navigation satellite system real-time kinematic (GNSS RTK) instrument (UniStrong Science and Technology Co., Ltd, Beijing, China). This instrument had a horizontal accuracy of 1.0 cm and a vertical accuracy of 2.0 cm.

2.2. UAV Image Acquisition

A MicaSense RedEdge 3 (MR) camera (MicaSense, Inc., Seattle, WA, USA) was mounted on the Matrice 600 hexacopter UAV (DJI, Shenzhen, China) to capture multispectral images. MR camera was a 12-bit multispectral imager with five channels (i.e., blue (475 ± 20 nm), green (560 ± 20 nm), red (668 ± 10 nm), NIR (840 ± 40 nm), and RE (717 ± 10 nm)) at 1.2 megapixel (1280 × 960 pixels) resolution. The spectral response curves of the five channels are shown in Figure 2, which was measured in reference to a previous study [33].
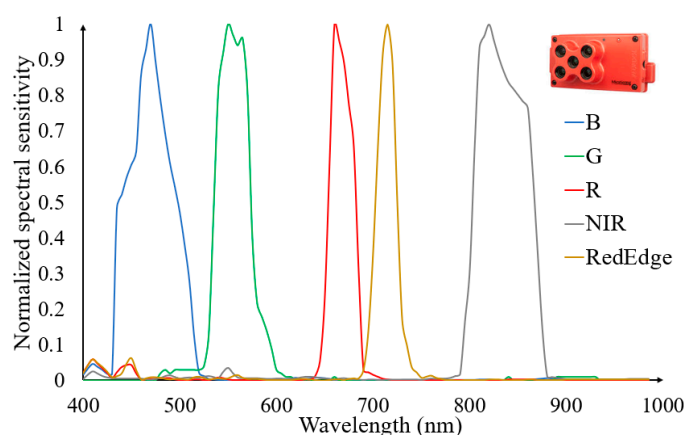

Figure 2. Spectral response curves of MicaSense RedEdge 3.

The UAV campaign was conducted under clear and calm weather conditions on December 13, 2018. Due to different experimental treatments, the growth stage of seedling rapeseed in the study area was slightly different, mainly in the 8-leaf to 10-leaf stage. Five flights were recorded between 10:00 and 14:00 h local time. An automatic mode was utilized to acquire multispectral images, which was recommended by MicaSense for normal exposure. The images were captured every 1 s with an 85.0% forward overlap and a 70.0% side overlap. The altitude, acquisition time, image processing time, and image GSD for each flight are given in Table 1. Finally, the acquired images were stored in 16-bit tiff format. Image processing time only included the time when images were automatically processed in the PIE-UAV software (Beijing Piesat Information Technology Co., Ltd., Beijing, China).

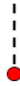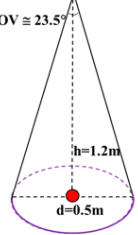**Table 1.** Parameters of data acquisition and processing for each flight.

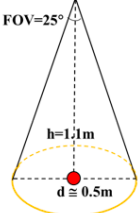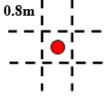| Flight Number	Altitude (m)	Image Acquisition Efficiency (min)	Number of Images	Image Processing Efficiency (min)	Image GSD (cm)
1	22	7.45	2400	100	1.35
2	29	4.02	1300	59	1.69
3	44	2.02	760	35	2.61
4	88	1.45	550	30	5.73
5	176	0.7	470	25	11.61

2.3. Field Data Acquisition

Ground sampling measurement was conducted on the same day as the UAV flights (Figure 3). The GS-NDVI readings were measured by a GreenSeeker®Handheld Crop Sensor (Trimble Navigation Limited, Sunnyvale, CA, USA) between 8:30 and 10:00 h. This instrument worked in an active remote sensing mode with a red wavelength range of 660 ± 25 nm and an NIR wavelength range of 780 ± 25 nm. The LAI and field-based hyperspectral reflectance data were obtained between 10:00 and 14:00 h. LAI readings were measured by an AccuPAR LP-80 plant canopy analyzer (Decagon Devices, Inc., Pullman, WA, USA). The instrument probe included 80 independent sensors spaced 1 cm apart to measure the photosynthetically active radiation intensity in the spectral range of 400–700 nm. Field-based hyperspectral reflectance was measured by a FieldSpec HandHeld 2 portable spectroradiometer (ASD Inc., Boulder, CO, USA). The ASD spectrometer was placed above the canopy to collect spectral data ranging from 325 to 1075 nm with a spectral resolution of <3 nm at 700 nm and a sampling interval of 1 nm. PH was measured by ruler with a minimum measurement unit of 1 mm. The GPS information at each sampling point was collected using the GNSS RTK receiver to associate the GS-NDVI, LAI, PH, and canopy reflectance data with the corresponding pixel locations in the UAV image. In this study, there were 90 plots, with a total of 180 sampling points which were all used for subsequent analysis. Descriptive statistics for ground measured data are shown in Table 2.

Table 2. Descriptive statistics for ground measured data.

Ground Measured Data	Sample Number	Min	Max	Mean	Std	CV (%)
NDVI measured by GreenSeeker (GS-NDVI)	180	0.53	0.78	0.72	0.06	8
Leaf area index (LAI)	180	0.41	6.15	3.17	1.20	38
Plant height (PH) (m)	180	0.10	0.63	0.35	0.12	34

Instrument	Picture	Measurement mode	Result type
GNSS RTK			GPS information
GreenSeeker		FOV ≅ 23.5° h=1.2m d=0.5m	GS-NDVI
ASD		FOV=25° h=1.1m d ≅ 0.5m	Ground hyperspectral reflectance
AccuPAR LP-80		0.8m	LAI

● Sampling point	○ FOV of GreenSeeker	○ FOV of ASD

Figure 3. Measurement mode of field-based sensors.

2.4. Data Pre-Processing

UAV-based multispectral images captured at the five different flights were processed separately. UAV multispectral images underwent a series of pre-processing including vignetting correction, lens distortion correction, image mosaicking, band registration, and radiometric calibration. Except for radiometric calibration, all the other pre-processing steps were performed using the PIE-UAV software (Beijing Piesat Information Technology Co., Ltd., Beijing, China). The relative differences between the initial and optimized internal camera parameters for flights 1 to 5 (Table 1) were small (0.49%, 0.50%, 0.60%, 0.61%, 0.94%, respectively), indicating that the initial parameters were accurate for image mosaicking. During the image mosaicking, the GPS information of the seven control points (Figure 1) measured by GNSS RTK was imported into the PIE-UAV to improve the spatial accuracy of the generated orthomosaics and point clouds. The GSDs of the five orthomosaics were 1.35, 1.69, 2.61, 5.73, and 11.61cm, respectively. Based on geo-referenced point clouds, the digital surface models (DSMs) were generated and exported in the TIF format with the same GSDs as the corresponding orthomosaics. Three calibration targets with nominal reflectance values of 11.0%, 31.0%, and 51.0% were placed in the study area and the photos of these calibration targets were captured by the MR sensor (Figure 1). The actual reflectance of the targets was measured with the ASD spectrometer and the digital numbers (DNs) of the corresponding areas were extracted from the orthomosaics. The DNs in the orthomosaics were then transformed into the reflectance by applying an empirical linear correction method [34]. Since the MicaSense RedEdge 3 camera produced an excellent linear response [35], the calibration equations of the MicaSense multispectral images were linear.

2.5. Regression Models of GS-NDVI and LAI

2.5.1. Estimation of GS-NDVI and LAI by UAV-VIs

In order to assess the effects of different GSD images on LAI and GS-NDVI estimation, some commonly used VIs were calculated by the formulas shown in Table 3. All the VIs were confirmed to be a useful indicator for vegetation growth. A circular buffer with a diameter of 50cm was generated for each sample, and the reflectance values of all the pixels within the area were averaged to represent the reflectance value for the sample. Then, the VIs were calculated in terms of different mathematical combinations of the reflectance. On this basis, regression models between each of the two ground measured crop parameters (GS-NDVI and LAI) and each of the UAV-VIs were established using MATLAB R2013a (MathWorks, Inc. Natick, Massachusetts, USA) and the coefficients of determination (R^2) were computed to assess the accuracy of the regression models.

Table 3. Formulas of nine different VIs.

VI	Formula [1]	NIR-VI	RE-VI	RGB-VI
Normalized difference vegetation Index	NDVI = (NIR − R) / (NIR + R) [36]	√		
Green Normalized Difference Vegetation Index	GNDVI = (NIR − G) / (NIR + G) [37]	√		
Difference Vegetation Index	DVI = NIR − R [38]	√		
Optimized Soil Adjusted Vegetation Index	OSAVI = (1 + 0.16) × (NIR-R) / (NIR + R + 0.16) [39]	√		
Excess Green index	ExG = 2G* − R* − B* [40]			√
Excess Red index	ExR=1.4R* − G* [41]			√
ExG − ExR	ExG − ExR [42]			√
Normalized Difference Index	NDI = (G-R)/(G + R) [43]			√
Red-edge Normalized Difference Vegetation Index	NDRE = (NIR-RE) / (NIR + RE) [44]		√	

[1]. Wavelengths of B, G, R, RE, and NIR were 474, 560, 668, 717, and 840 nm. G* = G / (R + G + B), R* = R/ (R + G + B), B* = B / (R + G + B).

2.5.2. Estimation of GS-NDVI and LAI by ASD-VIs

In order to evaluate the effect of VI types on canopy GS-NDVI and LAI estimation, the canopy reflectance measured by the ASD spectrometer was used to simulate the equivalent reflectance of the five bands by the following formula (1) [45]. The VIs (Table 3) were calculated based on the ASD data (ASD-VIs), and the coefficients of determination (R^2) between each of the two measured parameters (GS-NDVI and LAI) and each of the five ASD-VIs were also computed.

$$R_i = \frac{\sum_{\lambda_1}^{\lambda_2} S_\lambda \, R_\lambda \; d\lambda}{\sum_{\lambda_1}^{\lambda_2} R_\lambda \; d\lambda} \tag{1}$$

where R_i represents the reflectance corresponding to band i, and R_λ represents the reflectance measured by the spectroradiometer at wavelength λ. S_λ is the spectral response at wavelength λ of band i. λ_1 and λ_2 are the lower limit and upper limit wavelengths, respectively, for band i.

2.5.3. Estimation of LAI by UAV-VIs*PH$_{DSM}$

PH is a descriptor of plant growth. To get the PH information, the digital surface models (DSM) generated from point clouds at different GSDs were subtracted by a bare ground DSM [22] (Figure 4). The bare ground model was represented by a constant, which was the mean pixel value of bare soil in the DSM at a GSD of 1.35 cm. The bare soil was separated from NIR images at 1.35 cm GSD by using the Ostu method [46], which was reported to be able to efficiently and quickly determine the threshold and realize the segmentation of soil and seedling rapeseed [47]. Then, the average PH$_{DSM}$ within each circular buffer was calculated. On this basis, the VIs and PH were combined in the form of multiplication (VIs*PH$_{DSM}$) to establish LAI regression models, and the corresponding R^2 was also calculated in MATLAB R2013a.
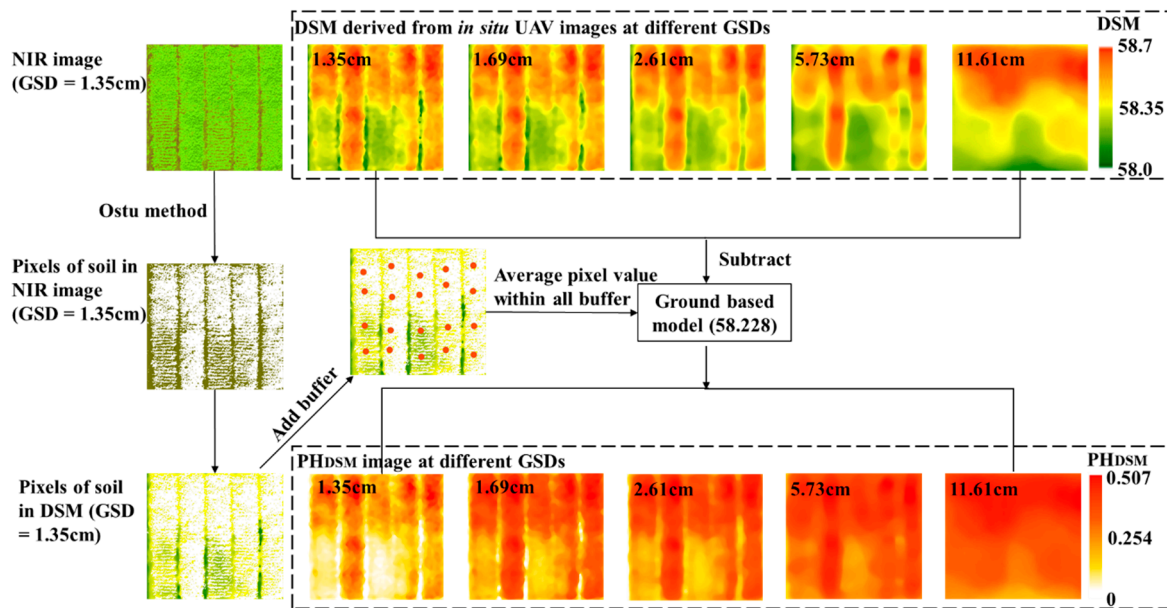
Figure 4. PH$_{DSM}$ at different ground sampling distances (GSDs). The red solid circles represented the buffers in Zonal Statistics as Table in ArcGIS for pixel value extraction.

3. Results

3.1. Performance of Different UAV-VIs for LAI and GS-NDVI Estimation

In this study, most VIs showed a linear relationship with GS-NDVI and an exponential relationship with LAI. However, the DVI showed a logarithmic relationship with GS-NDVI and LAI. The coefficients of determination and root mean square error (RMSE) between the two ground measured parameters (GS-NDVI and LAI) and the UAV-based VIs (UAV-VIs) under all GSDs are presented in Tables 4 and 5. Analysis results indicated that the NIR-VIs (OSAVI, NDVI, DVI, and GNDVI) and the RE-VI (NDRE) performed better than the RGB-VIs (ExG, ExR, ExG-ExR, and NDI). Among them, the VI with the strongest correlation with GS-NDVI was NDVI (R^2 = 0.826, RMSE=0.024). The NDRE exhibited a great performance for estimating both LAI and GS-NDVI, and it provided the most accurate estimation with an R^2 of 0.717 and RMSE of 0.695.

Table 4. Coefficients of determination between ground-measured parameters (GS-NDVI and LAI) and nine UAV-VIs [1].

VI Type	VI Name	R^2				
		GSD = 1.35 cm GS-NDVI/LAI	GSD = 1.69 cm GS-NDVI/LAI	GSD = 2.61 cm GS-NDVI/LAI	GSD = 5.73 cm GS-NDVI/LAI	GSD = 11.61 cm GS-NDVI/LAI
RGB-VIs	EXG	0.055/0.011	0.061/0.014	0.061/0.013	0.002/0.007	0.063/0.015
	EXR	0.292/0.166	0.317/0.186	0.313/0.179	0.237/0.101	0.308/0.209
	EXG-EXR	0.135/0.055	0.148/0.063	0.148/0.061	0.051/0.005	0.155/0.076
	NDI	0.344/0.208	0.384/0.240	0.362/0.218	0.292/0.137	0.280/0.184
RE-VI	NDRE	0.790/0.712	0.808/0.717	0.812/0.716	0.760/0.698	0.706/0.670
NIR-VIs	NDVI	0.817/0.664	0.826/0.666	0.821/0.651	0.804/0.661	0.664/0.609
	DVI	0.728/0.558	0.712/0.554	0.713/0.501	0.740/0.587	0.655/0.605
	GNDVI	0.787/0.714	0.794/0.704	0.806/0.700	0.763/0.699	0.630/0.627
	OSAVI	0.782/0.621	0.774/0.621	0.773/0.573	0.777/0.634	0.667/0.617
RGB-VIs			RE-VI		NIR-VIs	

[1]. The numbers before and after "/" were the R^2 for GS-NDVI and LAI with each UAV-VI, respectively.

Table 5. Root mean square error (RMSE) between ground-measured parameters (GS-NDVI and LAI) and nine UAV-VIs [1].

VI Type	VI Name	RMSE				
		GSD = 1.35 cm GS-NDVI/LAI	GSD = 1.69 cm GS-NDVI/LAI	GSD = 2.61 cm GS-NDVI/LAI	GSD = 5.73 cm GS-NDVI/LAI	GSD = 11.61 cm GS-NDVI/LAI
RGB-VIs	EXG	0.058/1.235	0.058/1.235	0.058/1.235	0.059/1.216	0.058/1.236
	EXR	0.050/1.208	0.049/1.205	0.049/1.205	0.052/1.219	0.049/1.191
	EXG-EXR	0.055/1.232	0.055/1.230	0.055/1.230	0.058/1.234	0.055/1.229
	NDI	0.048/1.193	0.047/1.184	0.047/1.190	0.050/1.207	0.050/1.200
RE-VI	NDRE	0.027/0.701	0.026/0.695	0.025/0.697	0.029/0.732	0.032/0.741
NIR-VIs	NDVI	0.025/0.742	0.024/0.744	0.025/0.769	0.026/0.767	0.034/0.777
	DVI	0.032/0.897	0.033/0.906	0.033/0.967	0.032/0.888	0.035/0.838
	GNDVI	0.027/0.696	0.027/0.704	0.026/0.714	0.029/0.731	0.036/0.772
	OSAVI	0.028/0.817	0.028/0.821	0.028/0.890	0.028/0.821	0.034/0.782
	RGB-VIs		RE-VI		NIR-VIs	

[1.] The numbers before and after "/" were the RMSE for GS-NDVI and LAI with each UAV-VI, respectively.

3.2. Performance of Different ASD-VIs for LAI and GS-NDVI Estimation

Our result indicated that the UAV-based NIR-VIs and RE-VI were better than the UAV-based RGB-VIs for LAI and GS-NDVI estimation. To further verify this result, the ASD reflectance was analyzed. As shown in Figure 5, the ASD-based NIR-VIs and RE-VI were obviously better than the ASD-based RGB-VIs. Among them, the ASD-VI with the strongest correlation with GS-NDVI and LAI was NDVI (R^2 = 0.797) and NDRE (R^2 = 0.624), respectively.
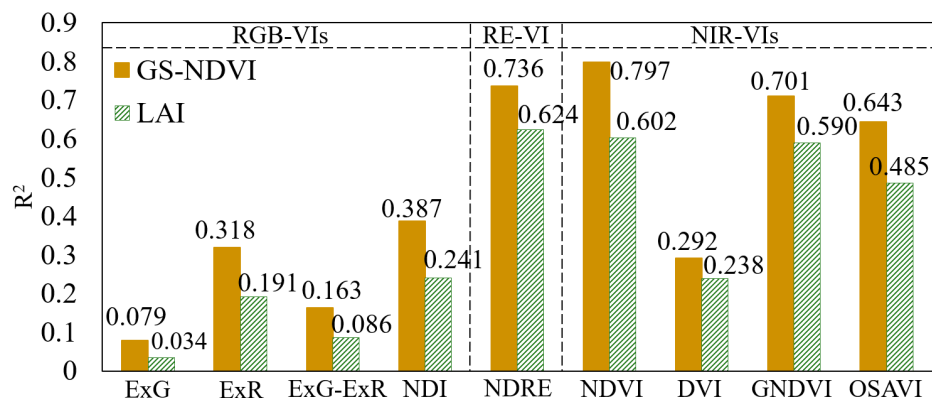
Figure 5. Correlation (R^2) between ground-measured parameters (GS-NDVI and LAI) and different ASD-VIs.

3.3. Performance of Optimal VIs under Different GSDs for LAI and GS-NDVI Estimation

The NDVI and NDRE that had the strongest correlations with GS-NDVI were selected for assessing the effects of different GSDs on GS-NDVI estimation (Table 4). The R^2 between GS-NDVI and either of the two VIs was almost unchanged when GSD increased from 1.35 to 5.73 cm ($R^2 > 0.76$ for NDRE, $R^2 > 0.804$ for NDVI), whereas a decrease in R^2 was observed at 11.61 cm GSD ($R^2 = 0.706$ for NDRE, $R^2 = 0.664$ for NDVI). The GNDVI and NDRE that had the strongest correlations with LAI were selected for evaluating the effects of different GSDs on LAI estimation. As shown in Table 4, R^2 between LAI and either VI also remained almost unchanged when GSD changed within 1.35–5.73 cm ($R^2 > 0.698$ for NDRE, $R^2 > 0.699$ for GNDVI), but it decreased sharply at 11.61 cm GSD ($R^2 = 0.670$ for NDRE, $R^2 = 0.627$ for GNDVI). Overall, the oversized GSD (11.61 cm) had an adverse effect on GS-NDVI and LAI estimation, while this trend was not obvious when the GSD was small (1.35-5.73 cm).

In addition, the difference between the VI derived from the UAV images (VItrue) and that from resampled images (VIres) was analyzed in this study (Figure 6). Resampled images were generated from the UAV image at 1.35 cm GSD by the nearest neighbor method [48]. Taking the optimal VI, NDRE, as an example, when GSD changed from 2.61 to 5.73 cm, NDREres was similar to NDREtrue with an R^2 larger than 0.956 and nRMSE less than 4.09%. However, at 11.61 cm GSD, the difference between NDREres and NDREtrue was obvious ($R^2 = 0.789$, nRMSE = 8.99%). Considering this issue, this study examined the effect of GSD on in situ VI generation by semivariograms. Taking the NDRE (best-performing VI) as an example, 1-m^2 images cropped from the NDRE images with different GSDs were used for semivariance calculation, in which the step size was set as 50 cm. As shown in Figure 7, the ratio of the nugget value (Co) to the base value (Sill) was less than 25.0% when the GSD was small (1.35–5.73 cm). However, when the GSD was 11.61 cm, the Co/Sill ratio was larger than 75.0%, indicating that there were many mixed pixels at 11.61 cm [49]. This might be the reason that the NDRE values of 180 samples were excessively concentrated within 0.5–0.6 at 11.61 cm GSD (Skewness = −1.398, Kurtosis = 1.599) (Figure 7).
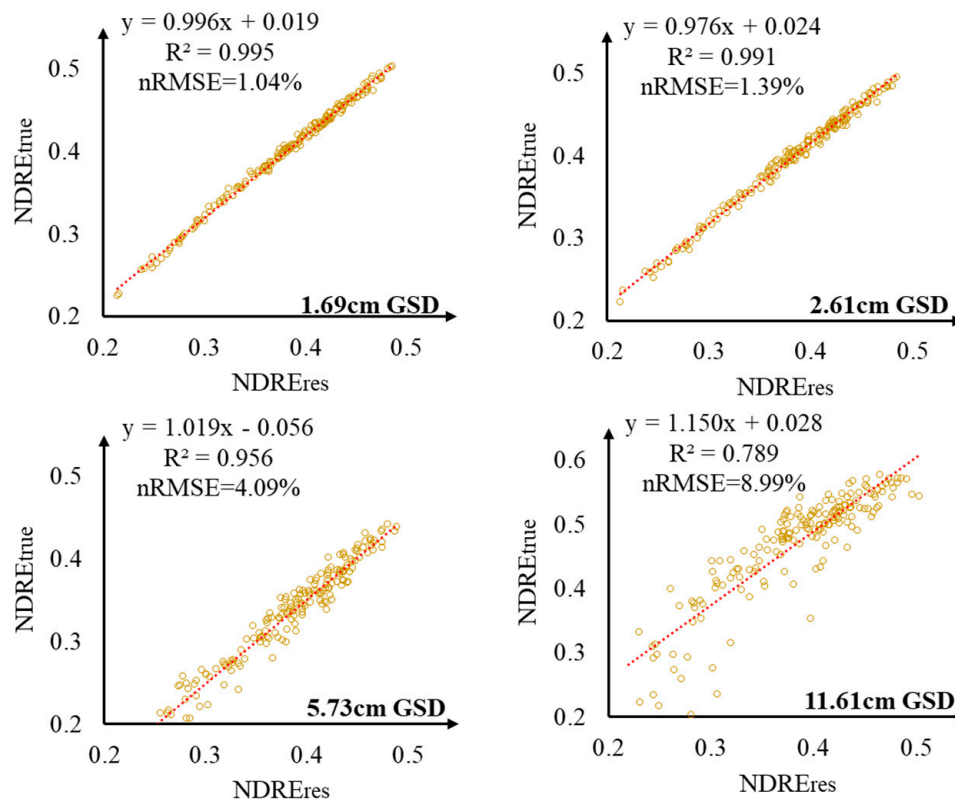

Figure 6. Scatter plots and regression lines of NDRE from in situ UAV image (NDREtrue) versus NDRE from resampled images (NDREres) at different GSDs.
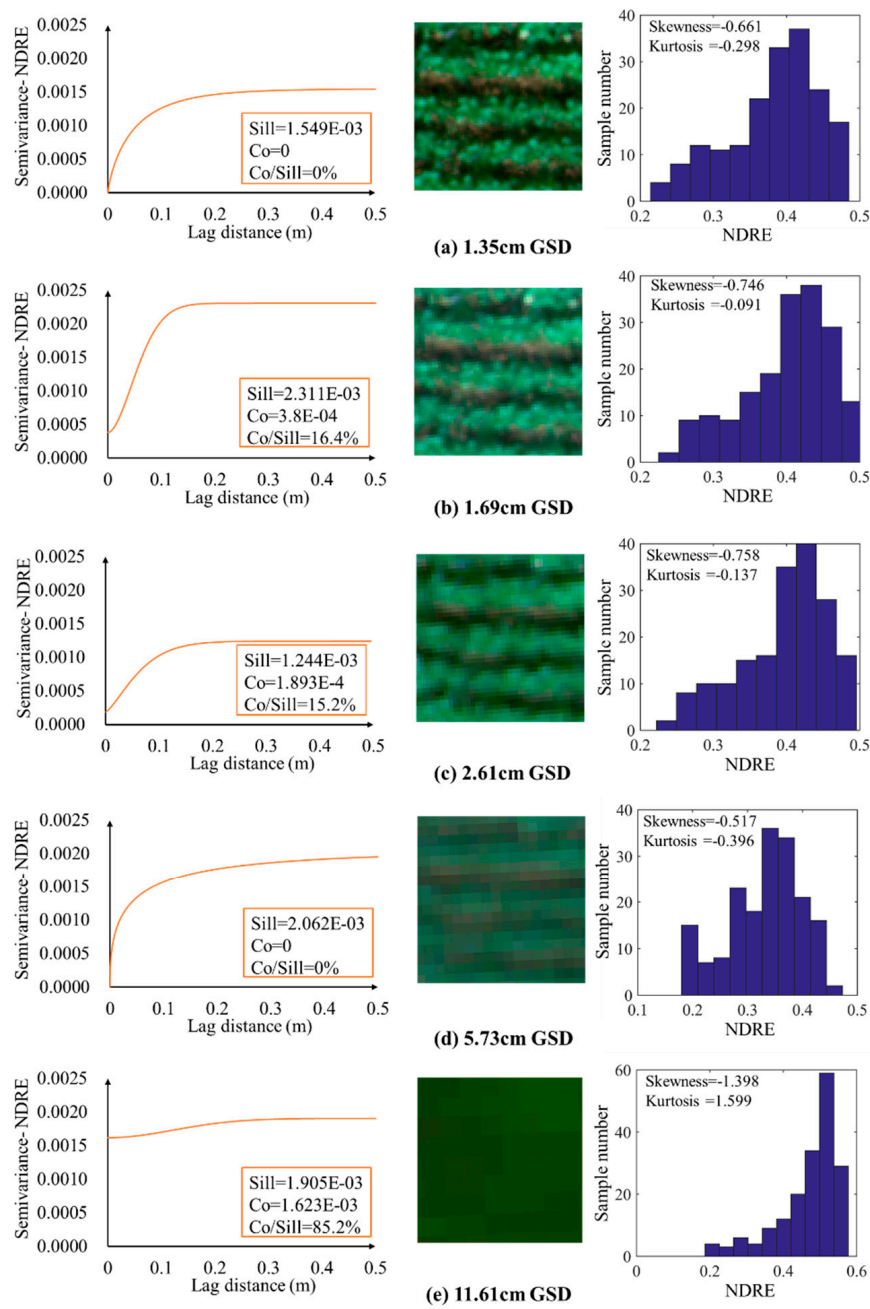
Figure 7. Semivariograms and distributions of NDRE values from in situ UAV images at different GSDs.

3.4. Performance of PH_{DSM} under Different GSDs for PH Estimation

The correlations between ground measured PH and DSM-derived PH_{DSM} are shown in Figure 8. The performance of PH estimation was similar at GSDs of 1.35 cm ($R^2 = 0.871$), 1.69 cm ($R^2 = 0.859$), and 2.61 cm ($R^2 = 0.856$), which were slightly better than that at 5.73 cm ($R^2 = 0.800$) and better than that at 11.61 cm ($R^2 = 0.351$).
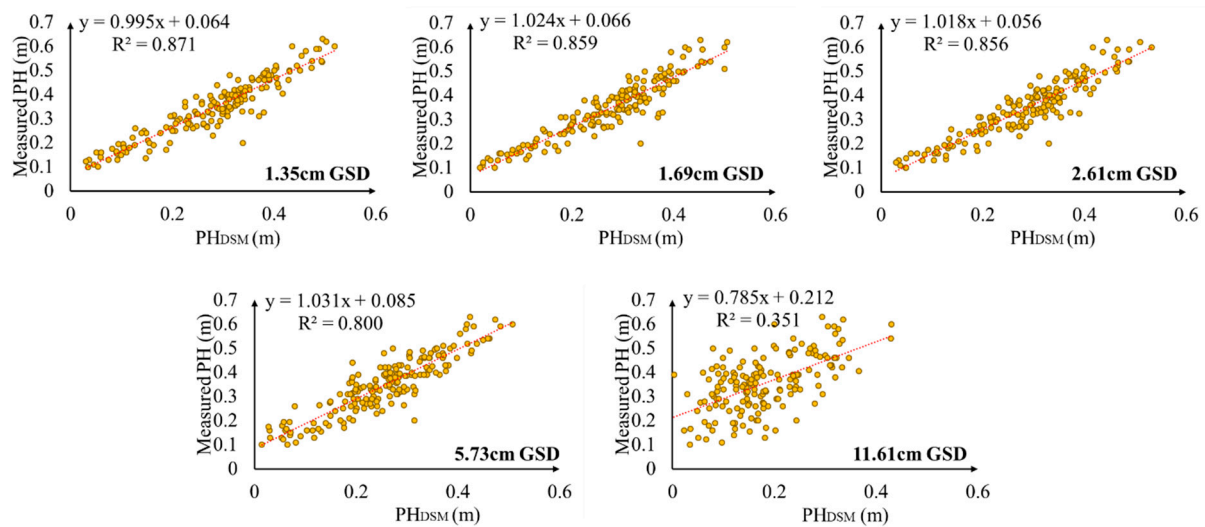
Figure 8. Relationships between ground-measured PH and DSM-derived PH (PH_{DSM}) at different GSDs.

3.5. Performance of VIs*PH_{DSM} under Different GSDs for LAI Estimation

Since NDRE exhibited the optimal performance among all the VIs, it was selected to represent the VI in the combination of VI*PH_{DSM} for LAI estimation. As shown in Figure 9, all the R^2 values between NDRE*PH_{DSM} and LAI were larger than 0.75 when GSD was between 1.35 and 2.61 cm. However, the R^2 showed a decreased trend at 5.73 cm ($R^2 = 0.717$) and 11.61 cm ($R^2 = 0.412$). The performance of NDRE* PH_{DSM} was better than that of NDRE alone when GSD was between 1.35 and 5.73 cm, but it was worse at 11.61 cm. In general, PH_{DSM} was helpful for LAI and GS-NDVI estimation when GSD was between 1.35 and 5.73 cm, while it was not useful for the estimation at 11.61 cm GSD.
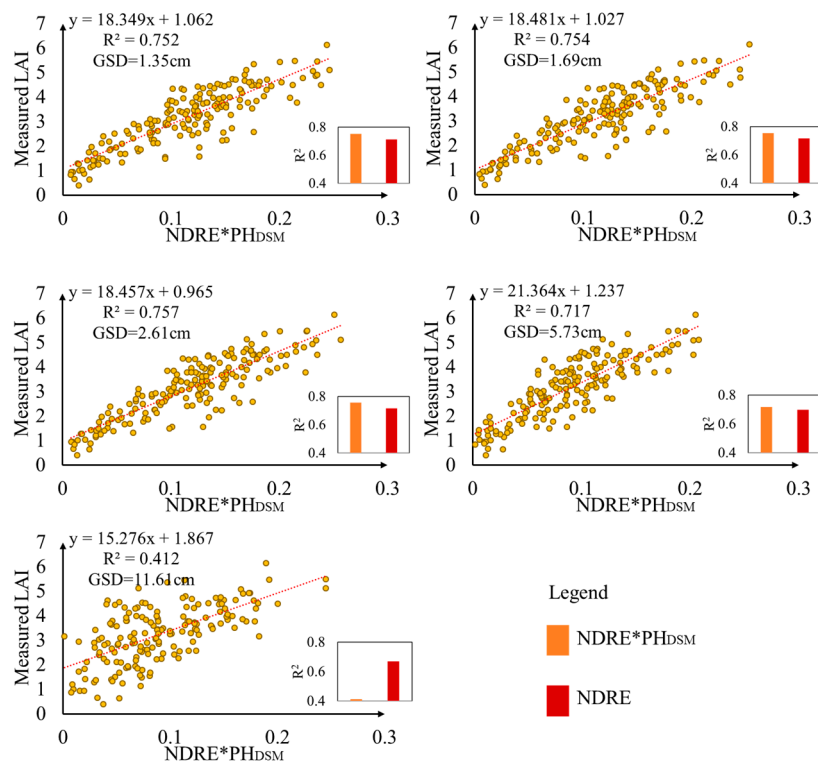

Figure 9. LAI estimation by NDRE*PH_{DSM} and NDRE. The scatter plots and regression lines show the relationship between NDRE*PH_{DSM} and ground-measured LAI. The histograms show the R^2 values between ground-measured LAI and either NDRE*PH_{DSM} or NDRE at different GSDs.

4. Discussion

4.1. Effect of VI Type on GS-NDVI and LAI Estimation

For GS-NDVI and LAI estimation, the ASD-based NIR-VIs and RE-VI were found to be better than the ASD-based RGB-VIs, which was consistent with the UAV-based result. On the one hand, the reason that GS-NDVI correlated better with RE-VI and NIR-VI was that they were computed from similar wavelengths. On the other hand, the RE and NIR bands were linked to plant structure, and thus to biophysical parameters such as LAI. In addition, the imaging quality was an important factor affecting the recording of spectral information [50,51], which might also affect the performance of RGB-VIs. In this study, we used an auto-exposure mode to acquire images using the multispectral sensor with its five channels working independently. Under this mode, the exposure parameters in each channel were adjusted according to the intensity of light reflected by ground objects. Therefore, the exposure parameters were determined by the reflection characteristics of the main ground objects, which might make the spectral information of monitoring objects difficult record well [52]. For example, the study area was covered with dry grass, cement surface, and other ground objects on the edge of the field. The light reflection intensity of these objects within the visible bands was higher than that of the rapeseed leaves (Figure 10). When image acquisition was performed at the edge of the field, a large proportion of image pixels would be occupied by the above-mentioned objects. In this case, the sensor automatically set a shorter exposure time or a smaller gain, resulting in a dark gray tone for rapeseed leaves in the visible images (Figure 11).
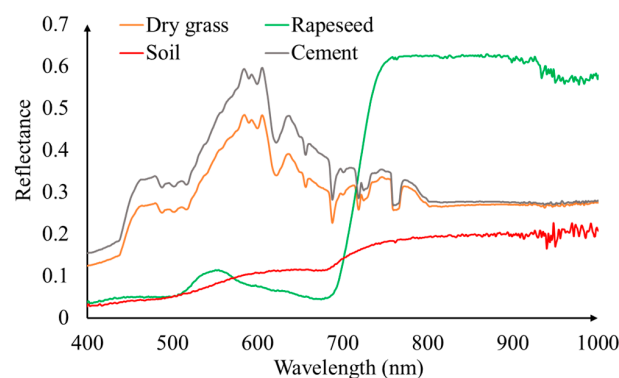

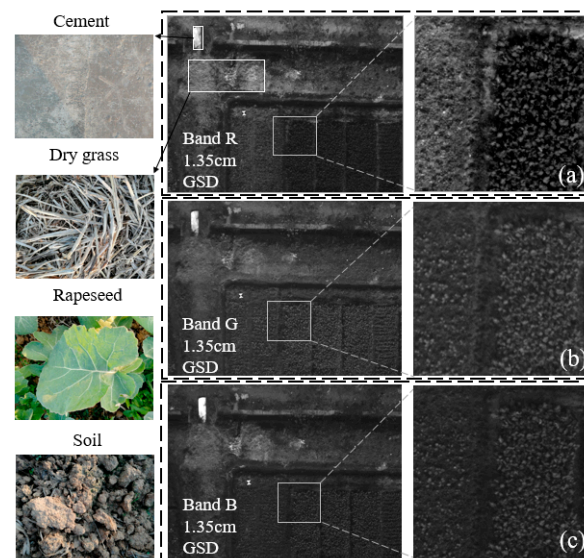**Figure 10.** Reflectance curves of different ground objects.

Figure 11. Visible band images at 1.35 cm GSD: (**a**) Red band; (**b**) Green band; (**c**) Blue band.

In this study, NDVI and GS-NDVI were computed from similar wavelengths. Therefore, both UAV-NDVI and ASD-NDVI exhibited the optimal performance for GS-NDVI estimation, which was consistent with the result of a previous study for rapeseed GS-NDVI estimation [53]. In addition, different treatments, including sowing dates, sowing densities, and straw incorporation in the study area, resulted in obvious differences in rapeseed growth and canopy structure (Table 2). NDRE was a VI that was less affected by the canopy structure [54], which might explain why this index had the best performance for LAI estimation.

4.2. Effect of VIs under Different GSDs on GS-NDVI and LAI Estimation

In this study, VItrue, with the large GSD of 11.61 cm, was found to have an adverse effect on GS-NDVI and LAI estimation, but this adverse effect was not obvious when the GSD was small (1.35–5.73 cm). Some previous studies reported that VIres was not affected by GSD [55]. Resampled images were always generated from original images by nearest neighbor, bilinear interpolation or cubic convolution [48,56,57], which represented a mathematical transformation process. Theoretically, the reflectance derived from resampled images would not change after radiometric calibration (Figure 12). Therefore, the VIs of the original UAV images should be similar to those of the resampled imagery.
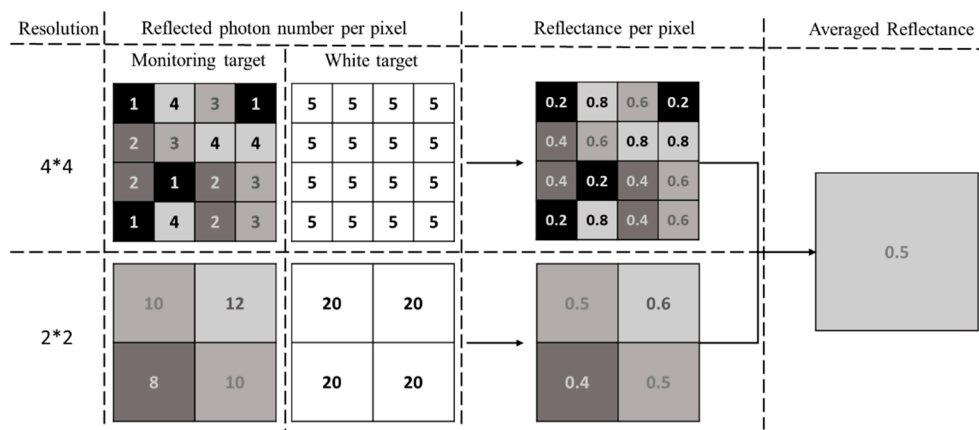

Figure 12. Reflectance generation process based on 2 × 2 and 4 × 4 pixels.

However, the VIres derived from a UAV image obtained at a certain flight height was not necessarily similar to the VIres from a resampled image with the same GSD (Figure 6). At the GSD of 11.61 cm, the difference between NDREres and NDREtrue was obvious and there were many mixed pixels. Due to the limitation of the gray level, the mixed pixels of in situ UAV images might result in large random errors in the acquired spectral information [25], making it difficult to discern the small spectral difference between the samples. This might be the reason that the NDRE values of 180 samples were excessively concentrated within 0.5–0.6, and why the LAI and GS-NDVI estimation results were undesirable at 11.61 cm.

4.3. Effect of PH_{DSM} under Different GSDs on LAI Estimation

Normally, the VIs were extracted from a rapeseed canopy, thus the lower leaves in a canopy might not be detected. Considering this, PH was utilized to make up the deficiency. Rapeseed is a dicotyledonous cruciferous crop [58]. As the main stem grows, new leaves will grow in branches (Figure 13), indicating that there is a relationship between PH and the number of middle- and lower-layer leaves. Therefore, when the GSD was between 1.35 and 5.73 cm, the LAI estimation was better with NDRE*PH_{DSM} than with NDRE (Figure 9). However, precise PH information could not be extracted from DSM images at 11.61 cm (Figure 8), resulting in an undesirable LAI estimation (Figure 9). Moreover, the performance of PH estimation was similar at small GSDs (1.35–2.61 cm), which was

slightly better than that at 5.73 cm. Therefore, the estimation performance by NDRE*PH$_{DSM}$ was best at small GSDs (1.35–2.61 cm), slightly worse at 5.73 cm and the worst at 11.61 cm.

Figure 13. Sketch map of vertical layers of a rapeseed plant at the seedling stage.

5. Conclusions

The effects of UAV-VIs and UAV-VIs*PH$_{DSM}$ at different GSDs on seedling rapeseed growth monitoring were assessed in this study. The results indicated that NDRE had a better performance for GS-NDVI and LAI estimation than other VIs, and that the NDRE*PH$_{DSM}$ derived from in situ UAV images with suitable spatial resolution (1.35–2.61 cm) could achieve a higher accuracy for LAI estimation than NDRE alone. Moreover, spatial resolution is directly proportional to UAV flight height and it affects the efficiency of image acquisition and processing. The image collection and processing time at 1.35 cm GSD was about three times as long as that at 2.61 cm. Therefore, selecting a relatively low spatial resolution that ensures monitoring accuracy can reduce time and cost. In this study, the optimal spatial resolution was determined to be about 2.61 cm for rapeseed LAI estimation.

The multispectral images with different GSDs were obtained through in situ collection in this study. The images with the actual GSDs were compared with images with the resampled GSDs to assess the effect of spatial resolution on rapeseed growth monitoring. Therefore, our findings could provide an accurate and practical reference for crop growth monitoring using UAV multispectral remote sensing technology.

Conflicts of Interest: The authors declare no conflict of interest.

References

1. Namany, S.; Al-Ansari, T.; Govindan, R. Optimisation of the energy, water, and food nexus for food security scenarios. *Comput. Chem. Eng.* **2019**, *129*, 106513. [CrossRef]
2. Zhang, C.; Kovacs, J.M. The application of small unmanned aerial systems for precision agriculture: A review. *Precis. Agric.* **2012**, *13*, 693–712. [CrossRef]

3. Jonckheere, I.; Fleck, S.; Nackaerts, K.; Muys, B.; Coppin, P.; Weiss, M.; Baret, F. Review of methods for in situ leaf area index determination. *Agric. For. Meteorol.* **2004**, *121*, 19–35. [CrossRef]

4. Nelson, B.W.; Mesquita, R.; Pereira, J.L.; De Souza, S.G.A.; Batista, G.T.; Couto, L.B. Allometric regressions for improved estimate of secondary forest biomass in the central Amazon. *For. Ecol. Manag.* **1999**, *117*, 149–167. [CrossRef]

5. Uddling, J.; Gelang-Alfredsson, J.; Piikki, K.; Pleijel, H. Evaluating the relationship between leaf chlorophyll concentration and SPAD-502 chlorophyll meter readings. *Photosynth. Res.* **2007**, *91*, 37–46. [CrossRef]

6. Pradhan, S.; Sehgal, V.K.; Bandyopadhyay, K.K.; Sahoo, R.N.; Panigrahi, P.; Parihar, C.M.; Jat, S.L. Comparison of vegetation indices from two ground based sensors. *J. Indian Soc. Remote Sens.* **2018**, *46*, 321–326. [CrossRef]

7. Zheng, H.; Cheng, T.; Yao, X.; Deng, X.; Tian, Y.; Cao, W.; Zhu, Y. Detection of rice phenology through time series analysis of ground-based spectral index data. *Field Crops Res.* **2016**, *198*, 131–139. [CrossRef]

8. Verhulst, N.; Govaerts, B.; Nelissen, V.; Sayre, K.D.; Crossa, J.; Raes, D.; Deckers, J. The effect of tillage, crop rotation and residue management on maize and wheat growth and development evaluated with an optical sensor. *Field Crops Res.* **2011**, *120*, 58–67. [CrossRef]

9. Marshall, M.; Thenkabail, P. Developing in situ non-destructive estimates of crop biomass to address issues of scale in remote sensing. *Remote Sens.* **2015**, *7*, 808–835. [CrossRef]

10. Jay, S.; Baret, F.; Dutartre, D.; Malatesta, G.; Héno, S.; Comar, A.; Weiss, M.; Maupas, F. Exploiting the centimeter resolution of UAV multispectral imagery to improve remote-sensing estimates of canopy structure and biochemistry in sugar beet crops. *Remote Sens. Environ.* **2018**, *231*, 110898. [CrossRef]

11. Kanning, M.; Kühling, I.; Trautz, D.; Jarmer, T. High-resolution UAV-based hyperspectral imagery for LAI and chlorophyll estimations from wheat for yield prediction. *Remote Sens.* **2018**, *10*, 2000. [CrossRef]

12. Peng, Y.; Li, Y.; Dai, C.; Fang, S.; Gong, Y.; Wu, X.; Zhu, R.; Liu, K. Remote prediction of yield based on LAI estimation in oilseed rape under different planting methods and nitrogen fertilizer applications. *Agric. For. Meteorol.* **2019**, *271*, 116–125. [CrossRef]

13. Li, S.; Yuan, F.; Ata-UI-Karim, S.T.; Zheng, H.; Cheng, T.; Liu, X.; Tian, Y.; Zhu, Y.; Cao, W.; Cao, Q. Combining color indices and textures of UAV-based digital imagery for rice LAI estimation. *Remote Sens.* **2019**, *11*, 1763. [CrossRef]

14. Aasen, H.; Burkart, A.; Bolten, A.; Bareth, G. Generating 3D hyperspectral information with lightweight UAV snapshot cameras for vegetation monitoring: From camera calibration to quality assurance. *ISPRS J. Photogramm. Remote Sens.* **2015**, *108*, 245–259. [CrossRef]

15. Verger, A.; Vigneau, N.; Chéron, C.; Gilliot, J.-M.; Comar, A.; Baret, F. Green area index from an unmanned aerial system over wheat and rapeseed crops. *Remote Sens. Environ.* **2014**, *152*, 654–664. [CrossRef]

16. Hunt, E.R.; Cavigelli, M.; Daughtry, C.S.T.; Mcmurtrey, J.E.; Walthall, C.L. Evaluation of digital photography from model aircraft for remote sensing of crop biomass and nitrogen status. *Precis. Agric.* **2005**, *6*, 359–378. [CrossRef]

17. Deng, L.; Mao, Z.; Li, X.; Hu, Z.; Duan, F.; Yan, Y. UAV-based multispectral remote sensing for precision agriculture: A comparison between different cameras. *ISPRS J. Photogramm. Remote Sens.* **2018**, *146*, 124–136. [CrossRef]

18. Yao, X.; Wang, N.; Liu, Y.; Cheng, T.; Tian, Y.; Chen, Q.; Zhu, Y. Estimation of wheat LAI at middle to high levels using unmanned aerial vehicle narrowband multispectral imagery. *Remote Sens.* **2017**, *9*, 1304. [CrossRef]

19. Liu, S.; Li, L.; Gao, W.; Zhang, Y.; Liu, Y.; Wang, S.; Lu, J. Diagnosis of nitrogen status in winter oilseed rape (Brassica Napus L.) using in-situ hyperspectral data and unmanned aerial vehicle (UAV) multispectral images. *Comput. Electron. Agric.* **2018**, *151*, 185–195. [CrossRef]

20. Zhou, K.; Cheng, T.; Zhu, Y.; Cao, W.; Ustin, S.L.; Zheng, H.; Yao, X.; Tian, Y. Assessing the impact of spatial resolution on the estimation of leaf nitrogen concentration over the full season of paddy rice using near-surface imaging spectroscopy Data. *Front. Plant Sci.* **2018**, *9*, 964. [CrossRef]

21. Jay, S.; Gorretta, N.; Morel, J.; Maupas, F.; Bendoula, R.; Rabatel, G.; Dutartre, D.; Comar, A.; Baret, F. Estimating leaf chlorophyll content in sugar beet canopies using millimeter- to centimeter-scale reflectance imagery. *Remote Sens. Environ.* **2017**, *198*, 173–186. [CrossRef]

22. Bendig, J.; Yu, K.; Aasen, H.; Bolten, A.; Bennertz, S.; Broscheit, J.; Gnyp, M.L.; Bareth, G. Combining UAV-based plant height from crop surface models, visible, and near infrared vegetation indices for biomass monitoring in barley. *Int. J. Appl. Earth Obs. Geoinformation* **2015**, *39*, 79–87. [CrossRef]

23. Yue, J.; Yang, G.; Li, C.; Li, Z.; Wang, Y.; Feng, H.; Xu, B. Estimation of winter wheat above-ground biomass using unmanned aerial vehicle-based snapshot hyperspectral sensor and crop height improved models. *Remote Sens.* **2017**, *9*, 708. [CrossRef]

24. Li, W.; Niu, Z.; Chen, H.; Li, D.; Wu, M.; Zhao, W. Remote estimation of canopy height and aboveground gbiomass of maize using high-resolution stereo images from a low-cost unmanned aerial vehicle system. *Ecol. Indic.* **2016**, *67*, 637–648. [CrossRef]

25. Croft, H.; Chen, J.M.; Zhang, Y.; Simic, A. Modelling leaf chlorophyll content in broadleaf and needle leaf canopies from ground, CASI, Landsat TM 5 and MERIS reflectance data. *Remote Sens. Environ.* **2013**, *133*, 128–140. [CrossRef]

26. Jayathunga, S.; Owari, T.; Tsuyuki, S. Digital aerial photogrammetry for uneven-aged forest management: Assessing the potential to reconstruct canopy structure and estimate living biomass. *Remote Sens.* **2019**, *11*, 338. [CrossRef]

27. Ming, D.; Yang, J.; Li, L.; Song, Z. Modified ALV for selecting the optimal spatial resolution and its scale effect on image classification accuracy. *Math. Comput. Model.* **2011**, *54*, 1061–1068. [CrossRef]

28. Lu, D. The potential and challenge of remote sensing-based biomass estimation. *Int. J. Remote Sens.* **2006**, *27*, 1297–1328. [CrossRef]

29. Singh, I.; Srivastava, A.K.; Chandna, P.; Gupta, R.K. Crop Sensors for Efficient Nitrogen Management in Sugarcane: Potential and Constraints. *Sugar Tech.* **2006**, *8*, 299–302. [CrossRef]

30. Teal, R.K.; Tubana, B.; Girma, K.; Freeman, K.W.; Arnall, D.B.; Walsh, O.; Raun, W.R. In-season prediction of corn grain yield potential using normalized difference vegetation index. *Agron. J.* **2006**, *98*, 1488–1494. [CrossRef]

31. Yao, Y.; Miao, Y.; Huang, S.; Gao, L.; Ma, X.; Zhao, G.; Jiang, R.; Chen, X.; Zhang, F.; Yu, K. Active canopy sensor-based precision N management strategy for rice. *Agron. Sustain. Dev.* **2012**, *32*, 925–933. [CrossRef]

32. Levy, P.E.; Jarvis, P.G. Direct and indirect measurements of LAI in millet and fallow Vegetation in HAPEX-Sahel. *Agric. For. Meteorol.* **1999**, *97*, 199–212. [CrossRef]

33. Jiang, J.; Liu, D.; Gu, J.; Süsstrunk, S. What is the space of spectral sensitivity functions for digital color cameras? In Proceedings of the 2013 IEEE Workshop on Applications of Computer Vision, Tampa, USA, 15–17 January 2013; pp. 168–179.

34. Zhou, X.; Zheng, H.B.; Xu, X.Q.; He, J.Y.; Ge, X.K.; Yao, X.; Cheng, T.; Zhu, Y.; Cao, W.X.; Tian, Y.C. Predicting grain yield in rice using multi-temporal vegetation indices from UAV-based multispectral and digital Imagery. *ISPRS J. Photogramm. Remote Sens.* **2017**, *130*, 246–255. [CrossRef]

35. Coburn, C.A.; Smith, A.M.; Logie, G.S.; Kennedy, P. Radiometric and spectral comparison of inexpensive camera systems used for remote sensing. *Int. J. Remote Sens.* **2018**, *39*, 4869–4890. [CrossRef]

36. Rouse, J., Jr.; Haas, R.H.; Schell, J.A.; Deering, D.W. Monitoring vegetation systems in the Great Plains with ERTS. *J. Water Resource Protection* **1974**, *351*, 309–317.

37. Gitelson, A.A.; Kaufman, Y.J.; Merzlyak, M.N. Use of a green channel in remote sensing of global vegetation from EOS-MODIS. *Remote Sens. Environ.* **1996**, *58*, 289–298. [CrossRef]

38. Richardson, A.J.; Everitt, J.H. Using spectral vegetation indices to estimate rangeland productivity. *Geocarto Int.* **1992**, *7*, 63–69. [CrossRef]

39. Rondeaux, G.; Steven, M.; Baret, F. Optimization of soil-adjusted vegetation indices. *Remote Sens. Environ.* **1996**, *55*, 95–107. [CrossRef]

40. Woebbecke, D.M.; Meyer, G.E.; Von Bargen, K.; Mortensen, D.A. Color indices for weed identification under various soil, residue, and lighting conditions. *Trans. ASAE* **1995**, *38*, 259–269. [CrossRef]

41. Meyer, G.E.; Hindman, T.W.; Laksmi, K. Machine vision detection parameters for plant species identification. In *Precision Agriculture and Biological Quality*; Society of Photo Optical: San Francisco, CA, USA, 1999; Volume 3543, pp. 327–336.

42. Meyer, G.E.; Neto, J.C. Verification of color vegetation indices for automated crop imaging applications. *Comput. Electron. Agric.* **2008**, *63*, 282–293. [CrossRef]

43. Bannari, A.; Morin, D.; Bonn, F.; Huete, A.R. A review of vegetation indices. *Remote Sens. Rev.* **1995**, *13*, 95–120. [CrossRef]

44. Gitelson, A.A.; Merzlyak, M.N. Spectral reflectance changes associated with autumn senescence of Aesculushippocatanum I and Hacer plantanoides I. leaves. Spectral features and relation to chlorophyll estimation. *J. Plant Physiol.* **1994**, *143*, 286–292. [CrossRef]

45. Hollberg, J.; Schellberg, J. Distinguishing intensity levels of grassland fertilization using vegetation indices. *Remote Sens.* **2017**, *9*, 81. [CrossRef]

46. Kim, D.W.; Yun, H.; Jeong, S.J.; Kwon, Y.S.; Kim, S.G.; Lee, W.; Kim, H.J. Modeling and testing of growth status for Chinese cabbage and white radish with UAV-based RGB imagery. *Remote Sens.* **2018**, *10*, 563. [CrossRef]

47. Zhao, B.; Zhang, J.; Yang, C.; Zhou, G.; Ding, Y.; Shi, Y.; Zhang, D.; Xie, J.; Liao, Q. Rapeseed seedling stand counting and seeding performance evaluation at two early growth stages based on unmanned aerial vehicle imagery. *Front. Plant Sci.* **2018**, *9*, 1362. [CrossRef]

48. Rizeei, H.M.; Pradhan, B. Urban mapping accuracy enhancement in high-rise built-up areas deployed by 3D-orthorectification correction from WorldView-3 and LiDAR imageries. *Remote Sens.* **2019**, *11*, 692. [CrossRef]

49. Xiaoyan, L.; Shuwen, Z.; Zongming, W.; Huilin, Z. Spatial variability and pattern analysis of soil properties in Dehui city, Jilin province. *J. Geogr. Sci.* **2004**, *14*, 503–511. [CrossRef]

50. Hasinoff, S.W.; Sharlet, D.; Geiss, R.; Adams, A.; Barron, J.T.; Kainz, F.; Chen, J.; Levoy, M. Burst photography for high dynamic range and low-light imaging on mobile cameras. *ACM Trans. Graph.* **2016**, *35*, 192. [CrossRef]

51. Monno, Y.; Teranaka, H.; Yoshizaki, K.; Tanaka, M.; Okutomi, M. Single-sensor RGB-NIR imaging: High-quality system design and prototype implementation. *IEEE Sens. J.* **2019**, *19*, 497–507. [CrossRef]

52. Nijland, W.; de Jong, R.; de Jong, S.M.; Wulder, M.A.; Bater, C.W.; Coops, N.C. Monitoring plant condition and phenology using infrared sensitive consumer grade digital cameras. *Agric. For. Meteorol.* **2014**, *184*, 98–106. [CrossRef]

53. Zhang, J.; Wang, C.; Yang, C.; Jiang, Z.; Zhou, G.; Wang, B.; Zhang, D.; You, L.; Xie, J. Evaluation of a UAV-mounted consumer grade camera with different spectral modifications and two handheld spectral sensors for rapeseed growth monitoring: Performance and influencing factors. *Precis. Agric.* **2020**, 1–29. [CrossRef]

54. Dong, T.; Liu, J.; Shang, J.; Qian, B.; Ma, B.; Kovacs, J.M.; Walters, D.; Jiao, X.; Geng, X.; Shi, Y. Assessment of red-edge vegetation indices for crop leaf area index estimation. *Remote Sens. Environ.* **2019**, *222*, 133–143. [CrossRef]

55. Dash, J.; Pearse, G.; Watt, M. UAV multispectral imagery can complement satellite data for monitoring forest health. *Remote Sens.* **2018**, *10*, 1216. [CrossRef]

56. Brell, M.; Segl, K.; Guanter, L.; Bookhagen, B. 3D hyperspectral point cloud generation: Fusing airborne laser scanning and hyperspectral imaging sensors for improved object-based information extraction. *ISPRS J. Photogramm. Remote Sens.* **2019**, *149*, 200–214. [CrossRef]

57. Zou, J.; Lan, J. A multiscale hierarchical model for sparse hyperspectral unmixing. *Remote Sens.* **2019**, *11*, 500. [CrossRef]

58. Downey, R.K. Agricultural and genetic potentials of cruciferous oilseed crops. *J. Am. Oil Chem. Soc.* **1971**, *48*, 718–722. [CrossRef]